

Material and geometric properties of hoop-type PZT interface for damage-sensitive impedance responses in prestressed tendon anchorage

Ngoc-Loi Dang^{1a}, Quang-Quang Pham^{2b} and Jeong-Tae Kim^{*2}

¹Urban Infrastructure Faculty, Mien Tay Construction University, Vinh Long 890000, Vietnam

²Department of Ocean Engineering, Pukyong National University, Nam-gu, Busan 48513, Korea

(Received May 17, 2020, Revised March 30, 2022, Accepted March 31, 2022)

Abstract. In this study, parametric analyses on a hoop-type PZT (lead-zirconate-titanate) interface are performed to estimate the effects of the PZT interface's materials and geometries on sensitivities of impedance responses under strand breakage. The paper provides a guideline for installing the PZT interface suitable in tendon anchorages for damage-sensitive impedance signatures. Firstly, the concept of the PZT interface-based impedance monitoring technique in prestressed tendon anchorage is briefly described. A FE (finite element) analysis is conducted on a multi-strands anchorage equipped with a hoop-type PZT interface for analyzing material and geometric effects. Various material properties, geometric sizes of the interface, and PZT sensor are simulated under two states of prestressing force for acquiring impedance responses. Changes in impedance signals are statistically quantified to analyze the effect of these factors on damage-sensitive impedance monitoring in the tendon anchorage. Finally, experimental analyses are performed to demonstrate the effects of materials and geometrical properties of the PZT interface on damage-sensitive impedance monitoring.

Keywords: damage-sensitive; impedance responses; material and geometric properties; prestressed tendon anchorage; PZT interface

1. Introduction

As the critical component of the prestressed concrete (PSC) structure, the tendon anchorage resists extreme prestress force before transferring it to the main structure (Cervenka *et al.* 2014). The instant loss of prestress force occurs due to the displacement in the anchoring subsystem during the installation of strands. Also, the time-dependent loss occurs due to strand corrosion, creep, and shrinkage of concrete anchorage (Tadros *et al.* 2003, Yang *et al.* 2020). The early detection of the prestress-loss is a critical issue to ensure structural integrity and to minimize the cost for long-term maintenance (Mehrabi *et al.* 2010).

Various structural health monitoring (SHM) methods have been developed for monitoring prestress-force levels based on contact-based sensors (Kim *et al.* 2010, Abdullah *et al.* 2015, Huynh

*Corresponding author, Professor, E-mail: idis@pknu.ac.kr

^aPh.D.

^bPh.D. Student

et al. 2017, Li *et al.* 2018, Hiba *et al.* 2019, Dang *et al.* 2020b, Kim *et al.* 2020). Vision-based cable force estimation has also been developed to monitor tensile forces of cables via deep learning algorithms and computer configurations (Kim *et al.* 2013, Tian *et al.* 2020). The SHM methods were applied to monitor long-term performances on real-scale PSC bridges under certain conditions (Yang *et al.* 2008, Ni *et al.* 2012, Asadollahi *et al.* 2017, Hu *et al.* 2017, Hwang *et al.* 2021). Vibration-based methods utilized modal parameters to identify the variation of structural characteristics induced by the change in prestress forces (Hamed *et al.* 2006, Ho *et al.* 2012). Moreover, vibration-based force monitoring has been proven successful for cable-stayed structures in which the cable-force is directly related to natural frequencies (Peeters *et al.* 2001, Ren *et al.* 2005, Zhang *et al.* 2020). However, modal vibration parameters are insensitive to minor structural damage. Also, the computer learning model should be generated to represent the baseline structural parameters, which demands a complex process for updating models (Ho *et al.* 2012, Ferrari *et al.* 2019). In addition, strain-based methods have been adopted to develop smart strands, in which fiber-optic sensors were embedded into the center wire of the 7-wire strand (Kim *et al.* 2012). Guided ultrasonic waves (GUWs) were applied when the end-tendons were free for placing transducers to excite and obtain GUWs (Moustafa *et al.* 2014). Meanwhile, other research groups have investigated effects of thermal actions on the monitoring results of the tower displacement in cable-stayed bridge (Yang *et al.* 2018b) and cable-stayed bridge girder deflection (Yang *et al.* 2018a).

For the last two decades, impedance-based methods have been implemented for various local health monitoring tasks (Kim *et al.* 2010, Min *et al.* 2016, Lu *et al.* 2018, Na 2018). For the methods, PZT (lead-zirconate-titanate) patches are installed onto monitored structures to acquire impedance signals via smart devices (e.g., smart probe (Lu *et al.* 2018), smart interface (Huynh *et al.* 2014), and smart aggregate (Wu *et al.* 2018)) or surface-mounted sensors (Yang *et al.* 2010, Min *et al.* 2016). Impedance features such as statistical metrics and frequency-shift extracted from impedance signals are utilized to estimate changes in structural conditions. The first implementation of the impedance-based method for monitoring prestress force in a real-scale PSC bridge was conducted by Kim *et al.* (2010). A PZT sensor is affixed on a steel plate of a tendon anchorage to acquire impedance responses under a series of prestress-force loss and structural damage. Also, Min *et al.* (2016) utilized changes in impedance features, which were measured from surface-mounted PZT sensors on a multi-strand anchorage, to estimate remaining tensile forces. In their studies, frequency bands over 100 kHz (demanding a high-cost impedance analyzer) were measured from surface-mounted PZT sensors (Kim *et al.* 2010, Min *et al.* 2016, Ai *et al.* 2018), which led to troubles in acquiring impedance signals and difficulties in determining damage-sensitive frequency ranges.

To deal with the above issues, a fixed type PZT interface was proposed by Nguyen and Kim (Nguyen *et al.* 2012). The fixed type interface was designed to synchronize lower resonant frequencies of the interface body that enhanced sensitive impedance responses. To improve practical usage, a portable PZT interface device was proposed as an alternative way for impedance measurement that enables the predetermination of impedance frequency bands (Huynh *et al.* 2014). Also, Dang *et al.* (2020b) proposed hoop-type PZT interfaces fitted to multi-strands anchorage for impedance measurement of local damaged strands. The feasibilities of those PZT interfaces for monitoring several scenarios in prestressed structures (e.g., prestress force and strand breakage) have been evaluated from lab-scaled experiments and numerical analyses.

The optimization of sensor placement and sensor size is a critical issue to realize an efficient structural health monitoring system. Optimal sensor placement has received attention from research communities since the SHM result is primarily affected by sensor placement (He *et al.* 2014, Zhou *et al.* 2015, Aloui *et al.* 2019, Hou *et al.* 2019, Dang *et al.* 2020a). Sensor designs, including sensor

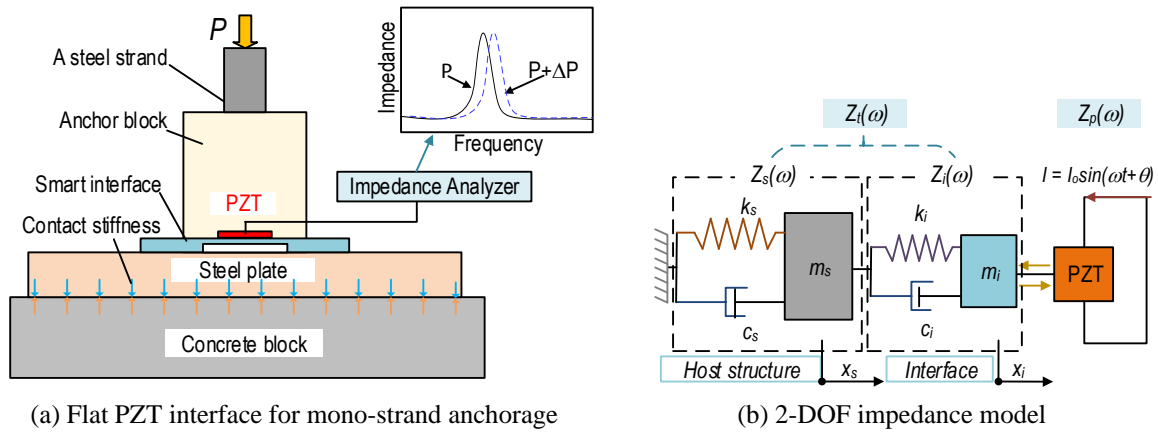


Fig. 1 Concept of impedance measurement via PZT interface at prestressed anchorage

sizes, materials, and protective sensor layer, also have significant effects on monitoring results (Yan *et al.* 2006, Yao *et al.* 2015, Huynh *et al.* 2019, Ai *et al.* 2020). Ai *et al.* (2020) investigated the effects of accelerator/retarder admixtures on hydration monitoring using impedance features of PZT sensors. Yang *et al.* (2021) optimized sensor design for SHM using a modified f-divergence objective functional. Yao *et al.* (2015) optimized the arrangement of the sensor array to improve the probability of damage detection. Also, Huynh *et al.* (2019) and Ryu *et al.* (2017) illustrated that the sensitivity of impedance features obtained from the PZT interface depended on the design parameters of the sensing devices. The effect of the PZT interface's characteristics on measured impedance signature should be quantitatively investigated to sensitively monitor incipient structural damage in tendon anchorage members.

In this study, parametric analyses on the hoop-type PZT interface are performed to estimate the effects of the PZT interface's materials and geometries on sensitivities of impedance variations-induced damaged strands. The study provides a guideline for installing the PZT interface suitable for damage-sensitive impedance responses in tendon anchorage. Firstly, the concept of the PZT interface-based impedance monitoring technique in prestressed tendon anchorage is briefly described. Secondly, a finite element (FE) model of 9-strands anchorage equipped with a hoop-type PZT interface is built using a commercial FE tool. Various material properties, geometric constants of PZT sensor, and interface are simulated to acquire impedance signatures under a damaged strand event. The RMSD (root-mean-square-deviation) damage metric is utilized to quantify the effects of these parameters on damage-sensitive impedance responses. Finally, experimental analyses are performed to demonstrate the effects of material and geometrical properties of the PZT and the interface on damage-sensitive impedance monitoring.

2. Impedance monitoring model for prestressed tendon anchorage

For impedance measurement in a prestressed tendon anchorage, a PZT interface technique is schematized in Fig. 1. The anchorage consists of a steel plate and an anchor block, which transfers the tensile force of the steel strand into the concrete structure. Contact stiffness is formed between the steel plate and the concrete block. The portable interface has two bonding parts and a deformable

part on which PZT is attached. The PZT interface is bonded on the anchorage surface to sense impedance responses from the interaction between the PZT interface and the structure (Huynh *et al.* 2014). As the prestress force P is altered, it leads to a change in the contact stiffness. The variation induces changes in structural parameters at the local anchorage zone.

In practice, impedance responses are calculated by a ratio of input harmonic voltage $V(\omega)$ and measured current electric current $I(\omega)$ using commercial impedance analyzers (e.g., HIOKI 3532) or impedance boards (e.g., AD 5933 EBZ (Na 2017)). The electromechanical impedance (Liang *et al.* 1994) of the system is a function of structural-mechanical (SM) impedance of the PZT patch $Z_a(\omega)$ and the one of PZT interface-anchorage, as shown in Eq. (1).

$$Z(\omega) = \frac{V(\omega)}{I(\omega)} = \left\{ i\omega A_p \left[\hat{\epsilon}_{33}^T - \frac{1}{\frac{Z_a(\omega)}{Z_t(\omega)} + 1} d_{3x}^2 \hat{Y}_{xx}^E \right] \right\}^{-1} \quad (1)$$

where A_p is geometric constants of the PZT patch; ω is the sweeping frequency of the excitation voltage; \hat{Y}_{xx}^E , $\hat{\epsilon}_{xx}^T$, and d_{3x} are the complex Young's modulus, the complex dielectric constant, and the piezoelectric coupling constant (in the x-direction) of the PZT patch at zero electric fields and zero stress, respectively.

The coupling interaction of interface-monitored structure can be modeled as an impedance model with two DOFs (degree of freedom), as shown in Fig. 1b. For the impedance model, a DOF presents the motions of tendon anchorage (x_s), and the other DOF refers to motions of the interface (x_i). The denotation k , c , and m are, respectively, the stiffness, damping coefficient, and mass. Also, the subscriptions s and i represent for the structure and the interface.

When external excitation at the PZT driving point has harmonic form $f_i(\omega) = F_i e^{i\omega t}$, the governing equation of the 2-DOFs model can be written (Huynh *et al.* 2017)

$$\begin{aligned} & \begin{bmatrix} m_i & 0 \\ 0 & m_s \end{bmatrix} \begin{Bmatrix} \ddot{x}_i \\ \ddot{x}_s \end{Bmatrix} + \begin{bmatrix} c_i & -c_i \\ -c_i & c_i + c_s \end{bmatrix} \begin{Bmatrix} \dot{x}_i \\ \dot{x}_s \end{Bmatrix} + \dots \\ & + \begin{bmatrix} k_i & -k_i \\ -k_i & k_i + k_s \end{bmatrix} \begin{Bmatrix} x_i \\ x_s \end{Bmatrix} = \begin{Bmatrix} F_i(\omega) \\ 0 \end{Bmatrix} \end{aligned} \quad (2)$$

Where $\ddot{x}_s, \dot{x}_s, x_s$ and $\ddot{x}_i, \dot{x}_i, x_i$ are the accelerations, velocities, and displacements corresponding to the motions of masses m_s and m_i , respectively. The steady solution can be written as $x_j = X_j e^{i\omega t}$ with $j=i, s$, X_i and X_s are, in general, complex quantities that depend on ω and system parameters. By solving Eq. (2), the value of X_i and X_s is presented in Eq. (3).

$$X_i = \frac{K_{22}(\omega)F_{i0}}{K_{11}(\omega)K_{22}(\omega) - K_{12}^2}; X_s = \frac{-K_{12}(\omega)F_{i0}}{K_{11}(\omega)K_{22}(\omega) - K_{12}^2} \quad (3)$$

where $K_{11} = -\omega^2 m_i + i\omega c_i + k_i$; $K_{12} = -i\omega c_i - k_i$, and $K_{22} = -\omega^2 m_s + i\omega(c_i + c_s) + (k_i + k_s)$ are dependent on modal properties of the interface-structure. The velocity of the interface at the PZT driving point can be obtained as

$$\dot{x}_s = i\omega X_i e^{i\omega t} = \frac{i\omega K_{22}(\omega)}{K_{11}(\omega)K_{22}(\omega) - K_{12}^2} f_i \quad (4)$$

The coupled structural-mechanical impedance $Z_t(\omega)$ of the structure-interface as functions of harmonic excitation and the velocity is shown as follows

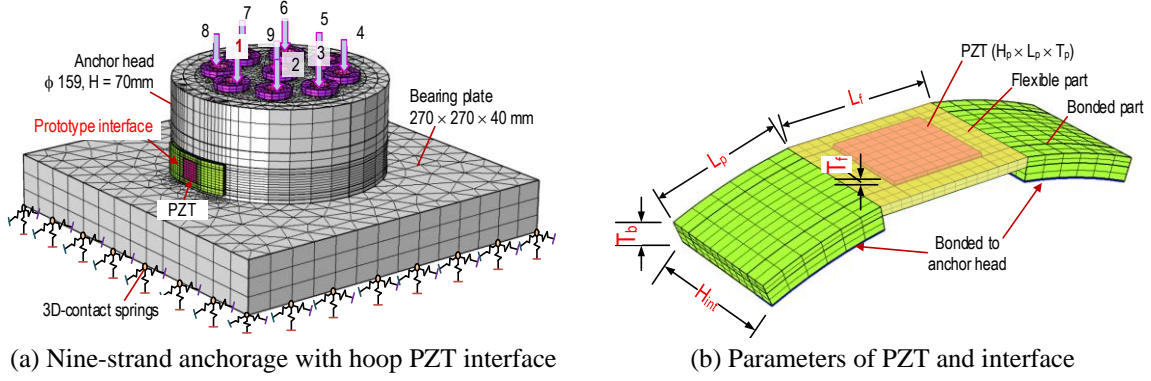


Fig. 2 FE model of 9-strand anchorage with PZT interface for impedance simulation

$$Z_t(\omega) = \frac{f_i(\omega)}{\dot{x}_i(\omega)} = \frac{K_{11}(\omega)K_{22}(\omega) - K_{12}^2(\omega)}{i\omega K_{22}(\omega)} \quad (5)$$

The impedance model consists of two resonant impedance peaks representing two coupling vibration motions of the PZT interface-monitored structure (Huynh *et al.* 2017, Dang *et al.* 2020b). These impedance peaks can be predetermined by adjusting geometric constants of the interface and the PZT sensor. As seen in Eq. (5), any changes in the monitored structure (e.g., prestress-loss) result in changes in the SM impedance $Z_t(\omega)$. When the structural impedance of the PZT patch is constant, structural damage can be detected by quantifying impedance signatures, as shown in Eq. (1).

Variations in impedance responses measured from the pristine and damage cases are statistically quantified using RMSD (root-mean-square-deviation) (Sun *et al.* 1995). In the study, real-part impedance signals were utilized for the calculation

$$RMSD(Z, Z^*) = \sqrt{\left(\frac{\sum_{j=1}^N [Z^*(\omega_j) - Z(\omega_j)]^2}{\sum_{j=1}^N [Z(\omega_j)]^2} \right)} \quad (6)$$

where N denotes the number of measured points in the frequency range, $Z(\omega_j)$ and $Z^*(\omega_j)$ are the real-part impedance signatures corresponding to the j^{th} sweeping point measured in the intact and the damage cases.

3. Parametric analysis of PZT interface

3.1 FE modeling of tendon anchorage with hoop-type PZT interface

As shown in Fig. 2, a finite element (FE) model of a multi-strand anchorage with a PZT interface was constructed using Comsol Multiphysics (a commercial FE tool) to analyze the effect of geometrical constants of the PZT sensor and the hoop-type interface. The anchorage system consists of a bearing plate ($270 \times 270 \times 40 \text{ mm}^3$) and an anchor head ($\phi 159 \text{ mm}$, 70-mm height) with nine conical wedges. An interface body was designed with a circumferential shape. It included two bonded parts (attached to the anchor head) and a flexible part equipped with a PZT patch (see Fig. 2(b)). The geometric parameters of PZT and interface were designed based on the size of the target anchorage (i.e., 9-strand anchor head) and the distribution of stress field change under a strand

breakage event. Also, the sizes of the PZT interface and its material were selected to enable that it can be implemented on a real structure (Dang *et al.* 2020b). As the prototype, a hoop-type PZT interface was positioned at the near-bottom and close to Strand 1 to sensitively catch stress variation induced by Strand 1 breakage. A thin layer with the thickness of $T_{bd}=0.1$ mm was used to simulate the contacts between the PZT-interface and the interface-anchor head.

In the FE model, the PZT interface was meshed with 64, 144, and 976 quadratic hexahedron elements for the PZT patch, bonding layers, and the interface body, respectively. As shown in Fig. 2(a), the anchorage meshed with 19754 quadratic tetrahedron elements for the anchor head-bearing plate and 2016 quadratic hexahedron elements for wedges. The spring constants with selected stiffness $k_x=k_y=0.5k_z$ (Dang *et al.* 2019) were implemented to simulate the remaining part of the reinforced concrete anchorage. It is noted that the spring constant was spring pressure per unit area, which was supported by the FE tool. This study focuses on analyzing the effects of material and geometric properties of the hoop-type PZT interface, so that the effects of spring stiffness on stress variation on the anchorage zone were ignorable. After try-and-error procedure, the spring stiffness was selected as $k_x=k_y=0.5k_z=2.5\times 10^{15}$ (N/m/m²). The damping loss factor was selected as 0.5% for the anchorage components (Bachmann *et al.* 2012).

3.2 Parametric analysis of PZT interface

The geometric constants of a baseline PZT interface were selected as follows: a) the PZT patch sized $H_p\times L_p\times T_p=15\times 15\times 0.51$ mm³, b) the deformable part of the interface sized $H_{int}\times W_f\times T_f=23\times 24\times 1.4$ mm³, and c) the two bonded parts of the interface sized $H_{int}\times W_b\times T_b=23\times 18\times 3.5$ mm³. The baseline PZT interface was set as a prototype when compared to other geometric constants. Moreover, this prototype was experimentally proved that it was sensitive to the damaged strands (Dang *et al.* 2020b). Parametric analysis scenarios were made to analyze the effect of material and geometrical conditions of the PZT interface (see Fig. 2(b)) on the measurement of damage-sensitive impedance responses of the multi-strands anchorage (see Fig. 2(a)).

Material properties of the PZT interface were examined only for the interface body. Note that the PZT patch was fixed as PZT 5A: $\rho=7750$ kg/m³ (mass density), Young's modulus $E=62.1$ (GPa), damping loss $\eta=0.0125$, dielectric loss factor $\delta=0.015$, Coupling Constant $d_{31}=-1.71\times 10^{-10}$ (m/V), and dielectric constant $\epsilon_{33}^T=1.53\times 10^{-8}$ (Farad/m). Moreover, geometrical properties of the PZT interface were examined for the sizes of the PZT patch and those of the interface (see Fig. 2(b)).

3.2.1 Material properties of interface body

Material properties of interface bodies were examined, as outlined in Table 1. Steel, aluminum, polypropylene plastic, and CFRP (carbon-fiber-reinforced polymers) were selected as four candidate

Table 1 Four materials selected for interface bodies

Parameters	Density ρ (kg/m ³)	Poisson's ratio ν	Young's modulus E , (GPa)	Tensile strength σ , (MPa)
Aluminum	2700	0.33	70	110
Structural steel	7850	0.33	200	450
CFRP	1700	0.33	145	1400~2000
Polypropylene plastic	1050	0.33	1.36	31

Table 2 Dimension of PZTs 1-9

Parameters	Notation	Value (mm)	Namely
Thickness	T_p	0.13, 0.27, 0.51, and 1.02	PZTs 1-4
Width, Height	$L_p=H_p$	11.7, 14.8, 17.4, 19.6 and 21.6	PZTs 5-9
	A_p/A_f	0.25, 0.4, 0.55, 0.70, and 0.85	

Table 3 Dimensions of interface for analyzing interface effects (unit: mm)

Parameters	Notation	Value (mm)	Namely
Thickness	T_f	0.8, 1.1, 1.4, 1.7, and 2.0	Interfaces 1-5
	T_b	2.7, 3.4, 4.1, and 4.8	Interfaces 6-9
Height	H_{int}	15, 19, 23, 27, and 31	Interfaces 10-14
Width	W_f	20, 24, 28, and 32	Interfaces 15-18

materials for the hoop-type interface. The steel interface, which is the same material as the anchor block, has higher yield strength to allow tensile stress up to 450 MPa. The aluminum interface has medium strength to allow tensile stress up to 110 MPa. The plastic interface, which is easy to fabricate, has the lowest strength to allow tensile stress up to 31 MPa (Omnexus 2017). Meanwhile, the CFRP interface has the highest strength to allow tensile stress up to 2000 MPa (Standards 2009).

3.2.2 Geometrical properties of PZT patch

As shown in Table 2, geometric constants of the PZT patch were examined as follows: a) the thickness of the PZT patch (T_p) and b) the coverage area of the PZT patch. The thickness of the PZT patch, T_p was simulated for four cases: 0.13, 0.27, 0.51, and 1.02 mm, namely PZTs 1-4. The coverage area of the PZT patch was simulated for five cases, namely PZTs 5-9. The ratio between the PZT patch area (A_p) and the interface's flexible section (A_f) was selected in the range of 0.25-0.85 with an interval of 0.15.

3.2.3 Geometrical properties of interface body

As shown in Table 3, geometric constants of the interface body were examined for the thickness of the flexible section T_f , the thickness of the bonded section T_b , the height of sensor interface H_{int} , and the length of flexible section L_f . Totally 18 cases were conducted for the impedance simulation (see Table 3). Specifically, the effect of the flexible-section thickness (namely Interfaces 1-5) was examined for $T_f=0.8-2.0$ mm with a 0.3-mm increment. The effect of the bonded-section thickness (Interfaces 6-9) was examined for $T_b=2.7-4.8$ mm with a 0.7-mm increment. The effect of the interface height (Interfaces 10-14) was tested for H_{int} 15-31 mm with a 4-mm increment. The flexible-section length (Interface 15-18) was analyzed for $L_f=20-32$ mm with a 4-mm increment.

Two cases of prestressing forces were simulated for each parametric analysis (material and geometric parameters). In the intact case, a force of 140 kN was applied to each of the nine wedges to simulate the baseline state of the structure. In the damage case, damage in Strand 1 was simulated by reducing the force on Wedge 1 to zero. Impedance responses were numerically acquired from the interaction between the PZT interface and the host structure by applying a 1V-harmonic voltage to the top surface of the PZT sensor.

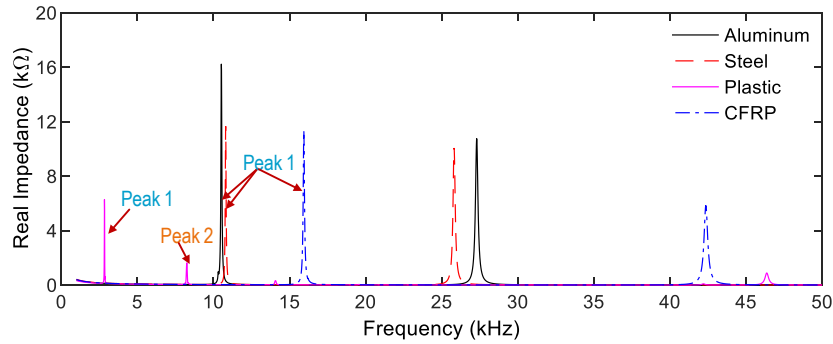


Fig. 3 Impedance signatures of four interface materials in frequency range 1-40 kHz: intact state

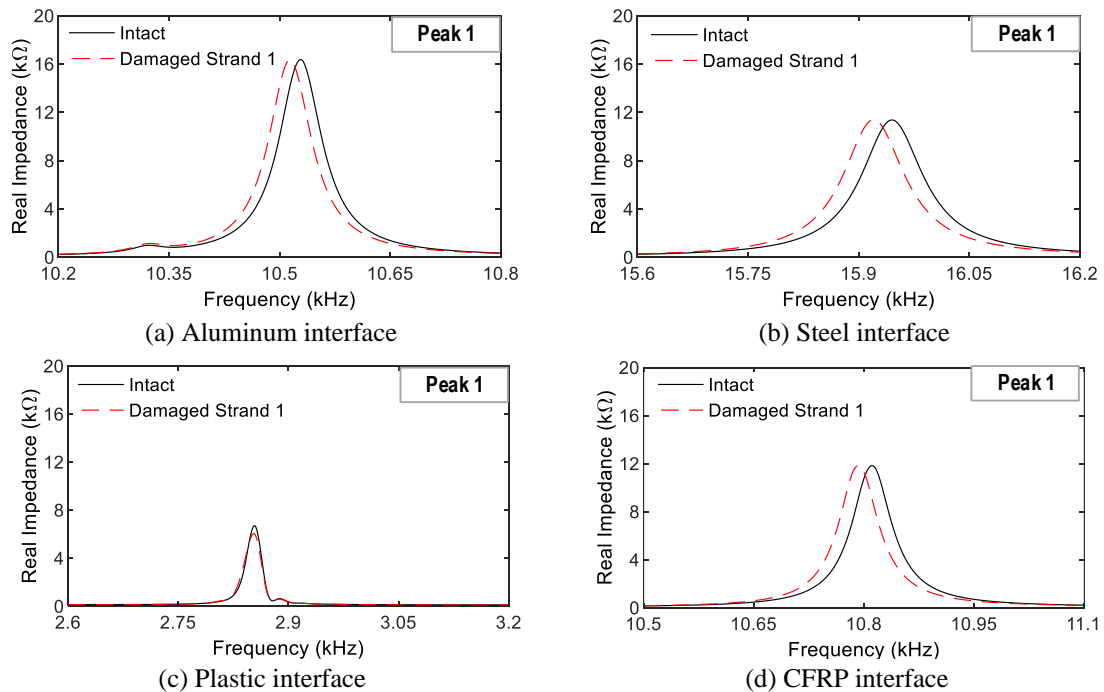


Fig. 4 Impedance responses of four interface materials in Peak 1's frequency range: Strand 1 breakage

4. Effects of selected parameters on damage-sensitive impedance responses

4.1 Sensitivities of impedance responses for four interface materials

Fig. 3 shows numerical impedance signatures of the sensor interfaces in the range 1-40 kHz for the aluminum, steel, plastic, and CFRP interfaces. For the four interface materials, two resonant impedance frequencies were found in the simulated range. The real-impedance magnitude of the aluminum interface exhibited the largest value. For Peak 1's resonant frequencies, the frequencies of aluminum and steel interfaces were close to each other (about 10.6 kHz). Moreover, the frequency of the CFRP interface was the highest (15.9 kHz), and the frequency of the plastic interface was the

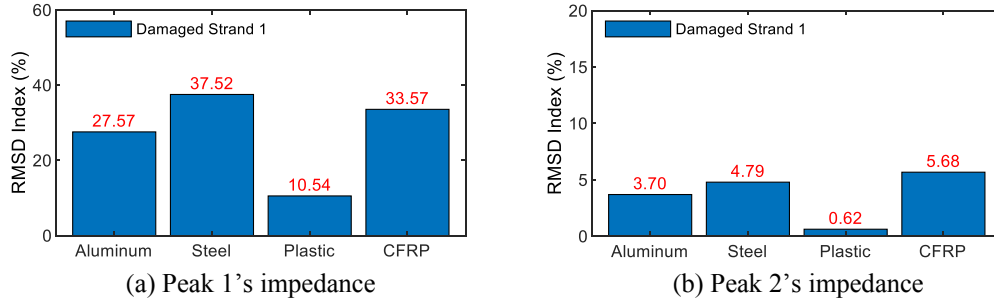


Fig. 5 Sensitivities of impedance signatures of four interface materials for damage detection

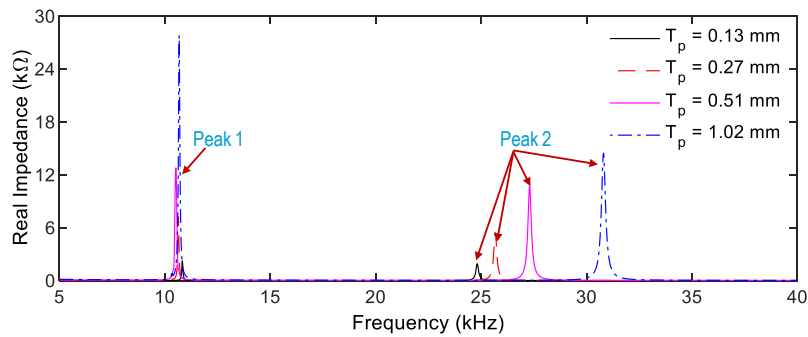


Fig. 6 Impedance signatures of PZTs 1-4 in the range 5-40 kHz: intact state

lowest (2.8 kHz).

For the Strand 1 breakage case, Fig. 4 shows impedance responses zoomed in Peak 1's frequency ranges for the four interface materials (e.g., 10.2-10.8 kHz for the aluminum interface). The impedance responses were clearly shifted leftward for the three PZT interfaces (aluminum, steel, or CFRP interface). In contrast, the variations in impedance signals of the plastic PZT interface (see Fig. 4(c)) were ignorable.

Statistical RMSD indices were calculated to quantify sensitivities of impedance responses of the four interface materials for damage detection, as presented in Fig. 5. The RMSD indices were calculated for resonant impedance signals of Peak 1 (0.6 kHz bandwidth) and Peak 2 (1.5 kHz bandwidth). For four interface materials, the RMSD indices of Peak 1 had a larger value than those of Peak 2. Specifically, the RMSD magnitude of the steel interface (37.5 %) was about 1.35 larger than that of the aluminum interface (27.6 %). The RMSD magnitude of the plastic interface had the smallest value. It is observed that the stiffer materials yielded higher sensitivity of impedance responses under the damaged strand.

4.2 Sensitivities of impedance responses for PZT-patch sizes

4.2.1 Effect of PZT-patch thickness

As shown in Fig. 6, impedance responses of the 5-40 kHz range were numerically gained for the intact state from the PZTs 1-4 (see Table 2). Two resonant peaks (Peaks 1-2) of impedance responses were observed in the range 10.4-11.1 kHz (Peak 1) and in the range 23-33 kHz (Peak 2). Among PZTs 1-4, PZT 4 (thickness of 1.02 mm) exhibited the largest impedance responses (28 kΩ for Peak

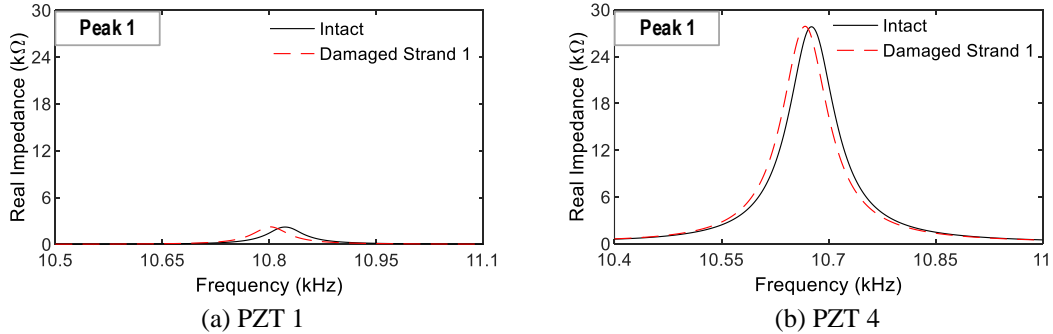


Fig. 7 Impedance responses of PZTs 1-4 zoomed in Peak 1's frequency range: Strand 1 breakage

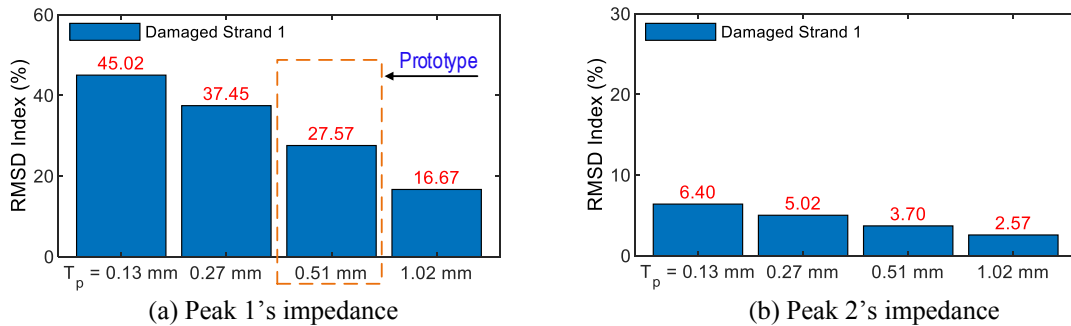


Fig. 8 Sensitivities of impedance signatures of PZTs 1-4 for damage detection

1). Meanwhile, PZT 1 presented the lowest impedance responses ($3 \text{ k}\Omega$ for Peak 1). The result suggested that the thicker PZT patch yielded better excitation of impedance signatures. For the damaged Strand 1, Fig. 7 shows Peak 1's impedance signals zoomed in the range 0.6 kHz : $10.5\text{-}11.1 \text{ kHz}$ for PZT 1 (see Fig. 7(a)) and $10.4\text{-}11 \text{ kHz}$ for PZT 4 (see Fig. 7(b)).

As shown in Fig. 8, RMSD indices were calculated to quantify sensitivities of impedance responses with respect to the four PZT-patch thicknesses. The RMSD indices of PZTs 1-4' impedance responses were computed for 0.6 kHz bandwidth of Peak 1's impedance and 1.5 kHz bandwidth of Peak 2's impedance. The RMSD indices (which are commonly used to indicate the sensitivities of damage detection) were reduced as the thickness of PZT patches increased. Notably, the PZT4's RMSD magnitude was the lowest, although it produced the highest magnitude of resonant impedance peaks. Based on the RMSD damage indicator and the capacity of PZT's excitation, the PZT patch's thickness should be 0.27 mm or 0.51 mm .

4.2.2 Effect of PZT-patch coverage area

Fig. 9 shows numerical impedance signatures in the range $5\text{-}35 \text{ kHz}$ obtained from the PZTs 5-9 (see Table 2) for the intact case. Two resonant peaks (Peaks 1-2) of impedance responses were observed: $10.5\text{-}11.5 \text{ kHz}$ for Peak 1 and $24.5\text{-}27.5 \text{ kHz}$ for Peak 2.

For the damaged Strand 1, Fig. 10 shows Peak 1's impedance signals in the range 0.6 kHz : $10.5\text{-}11.1 \text{ kHz}$ for PZT 5 (see Fig. 10(a)) and $9.8\text{-}10.4 \text{ kHz}$ for PZT 9 (see Fig. 10(b)). It is observed that the impedance responses of PZT 5 ($A_p/A_f=0.25$) were the most sensitive under the strand breakage event.

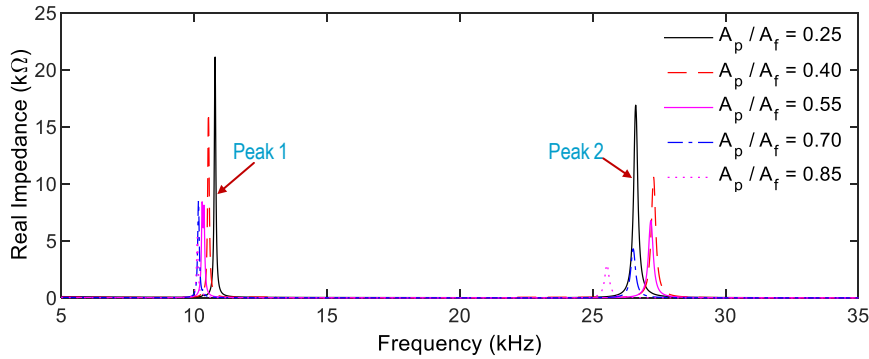


Fig. 9 Impedance signatures of PZTs 5-9 in the range 5-35 kHz: intact state

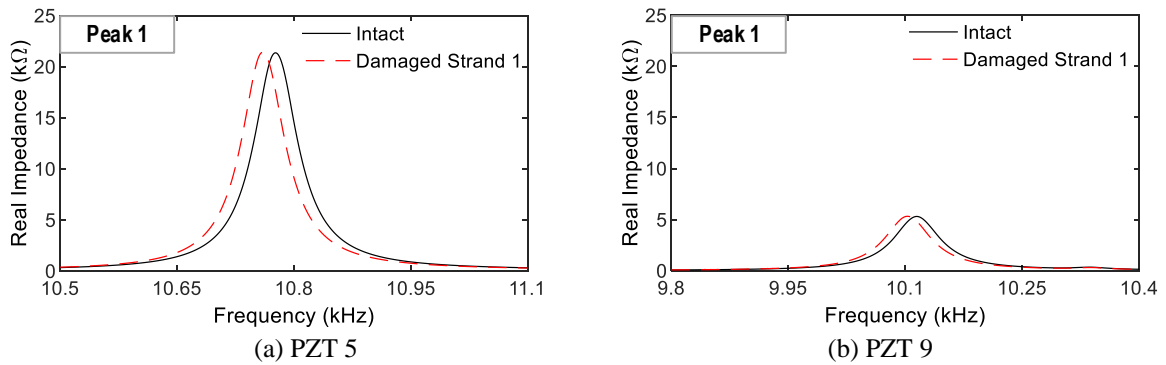


Fig. 10 Impedance signatures of PZTs 5-9 zoomed in Peak 1's frequency range: Strand 1 breakage

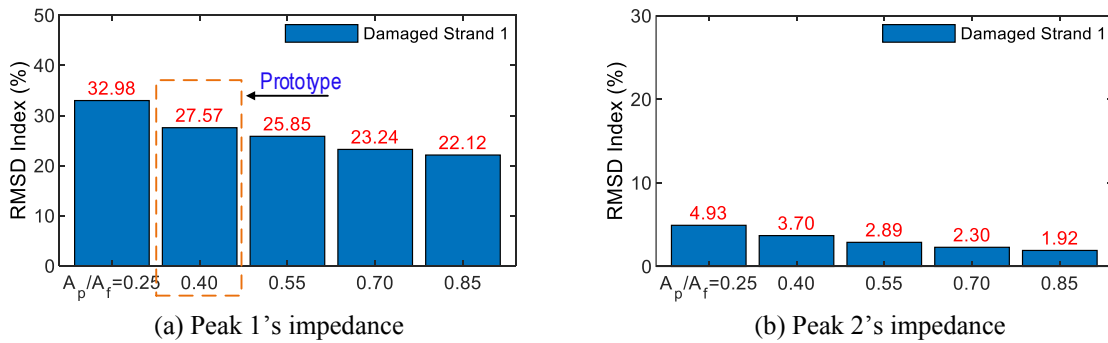


Fig. 11 Sensitivities of impedance signatures of PZTs 5-9 for damage detection

Fig. 11 shows RMSD indices of PZTs 5-9 calculated for 0.6 kHz bandwidth of Peak 1's impedance and 1.5 kHz bandwidth of Peak 2's impedance. The RMSD indices were linearly decreased once the PZT covering areas were reduced for two impedance peaks. Notably, PZT 5's RMSD magnitude was about 1.5 times larger than that of PZT 9. The result suggested that the ratio A_p/A_f should be lower than 0.5 to maximize the performance of PZT for damage detection.

4.3 Sensitivities of impedance responses for interface geometries

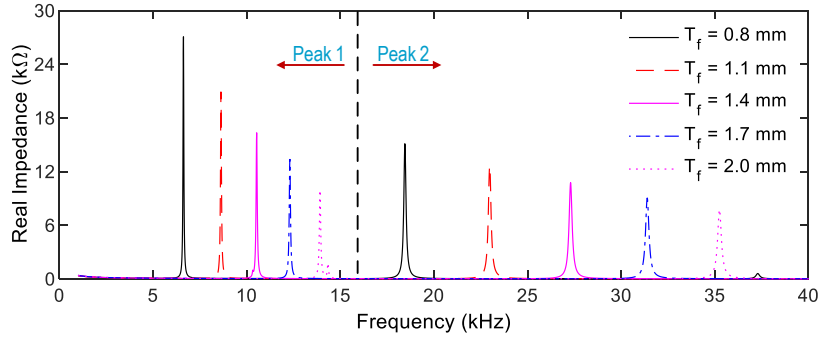


Fig. 12 Impedance signatures of Interfaces 1-5 in the range 2-40 kHz: intact state

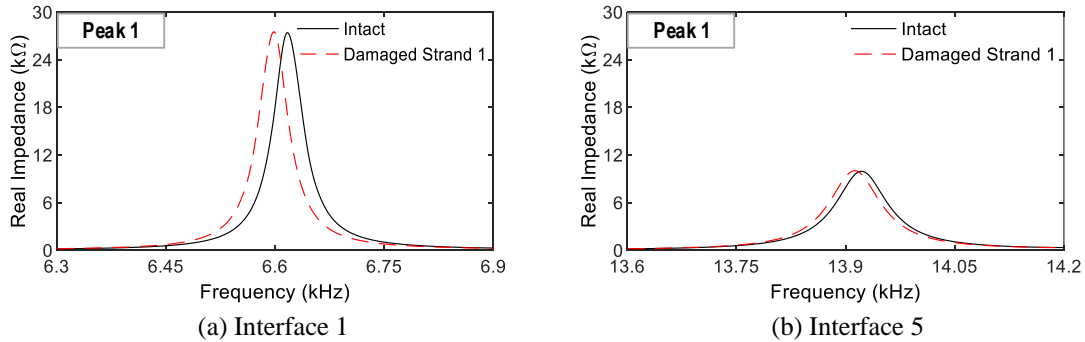


Fig. 13 Impedance signatures of Interfaces 1-5 zoomed in Peak 1's frequency range: Strand 1 breakage

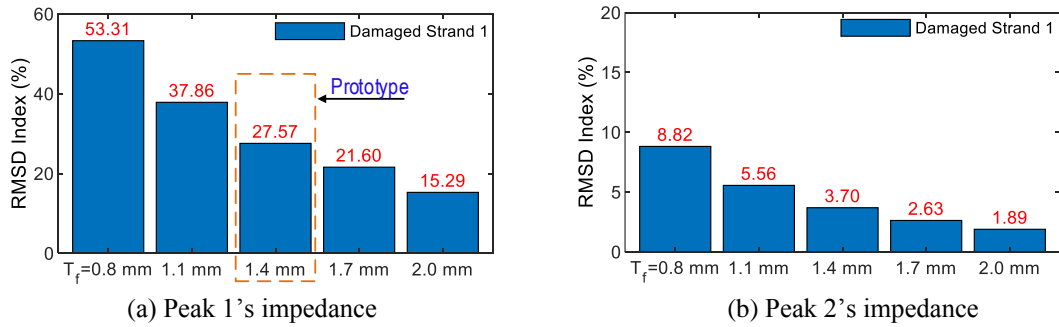


Fig. 14 Sensitivities of impedance signatures of Interfaces 1-5 for damage detection

4.3.1 Effect of flexible-section thickness

As shown in Fig. 12, impedance signatures of 1-40 kHz range were obtained for the intact state from Interfaces 1-5 (see Table 3). Two resonant peaks (Peaks 1-2) of impedance signatures were observed in the range 5-16 kHz for Peak 1 and 16-40 kHz for Peak 2. The frequencies were leftward shifted and decrease in real-impedance magnitude when T_f (flexible-section thickness of interface) increased from 0.8-2.0 mm (i.e., Interfaces 1-5).

For the damaged Strand 1, Fig. 13 shows resonant impedance signals of Peak 1 zoomed in the range 0.6 kHz: 6.3-6.9 kHz for Interface 1 and 13.6-14.2 kHz for Interface 5. Impedance signatures of Interface 1 (see Fig. 13(a)) had higher variation than that of Interface 5 (see Fig. 13(b)).

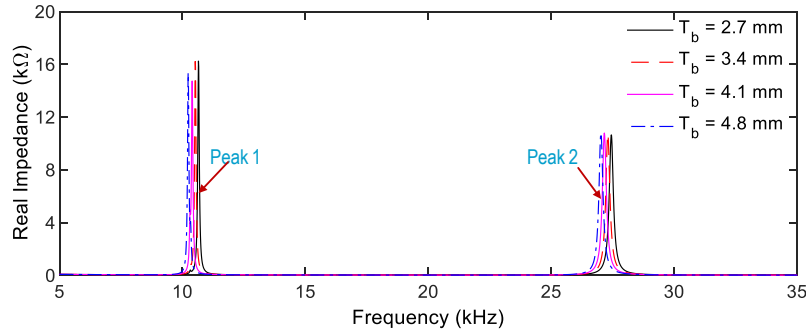


Fig. 15 Impedance signatures of Interfaces 6-9 in the range 5-35 kHz: intact state

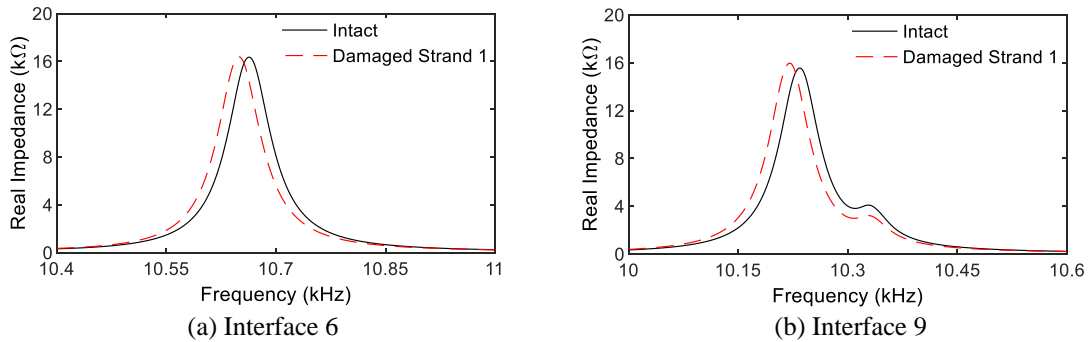


Fig. 16 Impedance signatures of Interfaces 6-9 zoomed in Peak 1's frequency range: Strand 1 breakage

As shown in Fig. 14, RMSD indices of Interfaces 1-5' impedance responses were calculated for 0.6 kHz-bandwidth of Peak 1's impedance and 1.5 kHz-bandwidth of Peak 2's impedance. As observed in the figure, when flexible-section thickness linearly increased, RMSD magnitudes decreased. Specifically, for Peak 1's impedance, Interface 1's RMSD magnitude (53.3 %) was quite larger than that of Interface 3 (27.6 %) or Interface 5 (15.3 %). It demonstrated that the flexible-section thickness had the primary effect on damage-sensitive impedance signatures of the hoop-type PZT interface.

4.3.2 Effect of bonding-section thickness

Fig. 15 shows numerical impedance signatures in the range 5-35 kHz obtained from Interfaces 6-9 (see Table 3) in the intact state. Two resonant peaks (Peaks 1-2) of impedance responses were observed in the range of 9.5-11.0 kHz for Peak 1 and 26-28.5 kHz for Peak 2. The resonant impedance frequencies varied slightly as the thickness of the bonded section increased from 2.7 mm to 4.8 mm (i.e., Interfaces 6-9).

For the damaged Strand 1, Fig. 16 illustrates impedance signals of Peak 1 zoomed in the range 0.6 kHz: 10.4-11.0 kHz for Interface 6 (see Fig. 16(a)) and 10-10.6 kHz for Interface 9 (see Fig. 16(b)). The resonant frequency was leftward shifted, but variations in impedance signals were slightly different.

As shown in Fig. 17, RMSD indices of Interfaces 6-9' impedance responses were computed for 0.6 kHz-bandwidth of Peak 1's impedance and 1.5 kHz-bandwidth of Peak 2's impedance. There were no significant differences in RMSD indices of Interfaces 6-9 for the two impedance peaks.

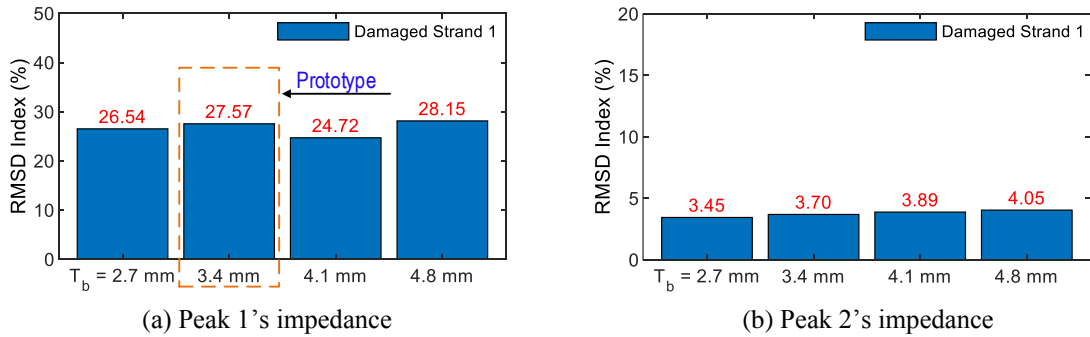


Fig. 17 Sensitivities of impedance signatures of Interfaces 6-9 for damage detection

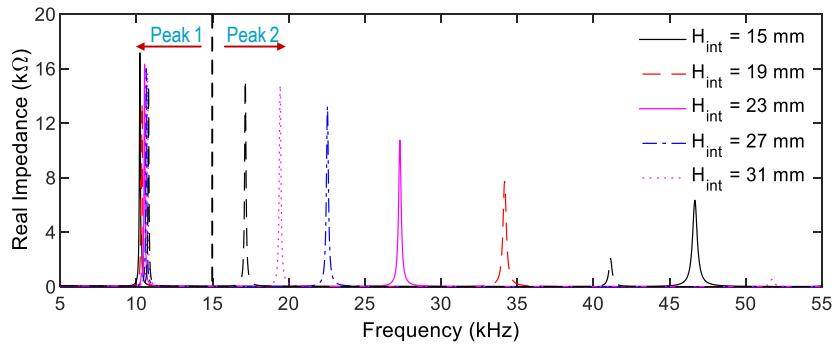


Fig. 18 Impedance signatures of Interfaces 10-14 in the range 5-55 kHz: intact state

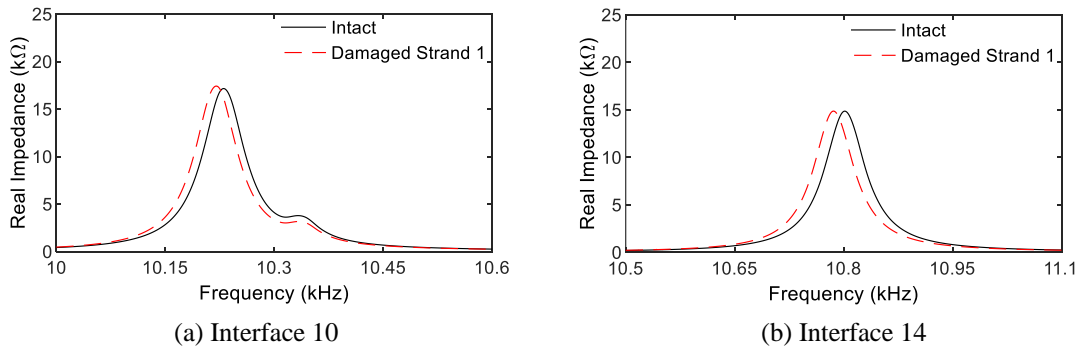


Fig. 19 Impedance signatures of Interfaces 10-14 zoom in Peak 1's frequency range: Strand 1 breakage

The result revealed that the bonding-section thickness of the hoop interface had relatively little effect on the detection result of strand breakage.

4.3.3 Effect of interface height

Fig. 18 illustrates impedance signatures of Interfaces 10-14 (see Table 3) in the range 5-55 kHz for the intact state. Two distinguishing resonant peaks (Peaks 1-2) of impedance signals were observed in the range 5-13 kHz for Peak 1 and 16-50 kHz for Peak 2. Peak 1's impedance frequencies were little varied as the interface height increased from 15 mm to 31 mm. Meanwhile,

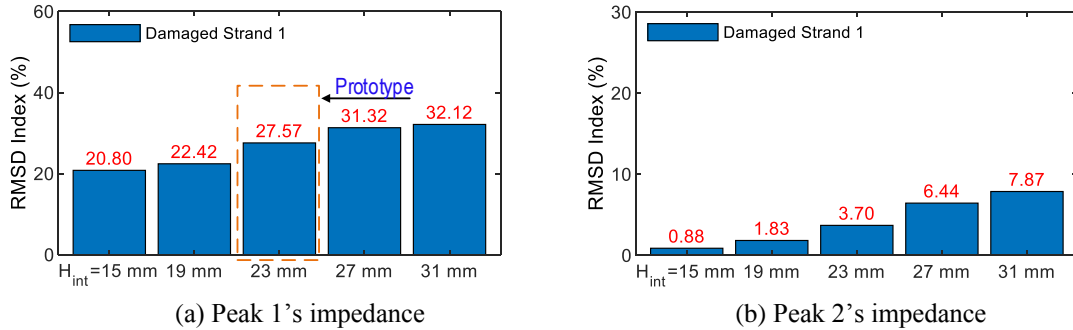


Fig. 20 Sensitivities of impedance signatures of Interfaces 10-14 for damage detection

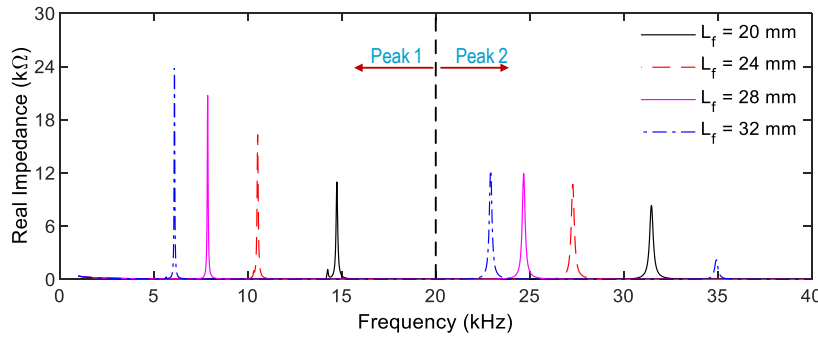


Fig. 21 Impedance signatures of Interfaces 15-18 in the range 2-40 kHz: intact state

those of Peak 2 decreased from 47 kHz (Interface 10) to 17.5 kHz (Interface 14).

For the damaged Strand 1, Fig. 19 shows impedance signatures of Peak 1 zoomed in the range: 10-10.6 kHz for Interfaces 10 (see Fig. 19(a)) and 10.5-11.1 kHz for Interface 14 (see Fig. 19(b)). Variations in impedance signatures-induced strand breakage were insignificantly different.

Fig. 20 shows the Interfaces 10-14' RMSD indices were calculated for 0.6 kHz-bandwidth of Peak 1's impedance and 1.5 kHz-bandwidth of Peak 2's impedance. The RMSD indicator was slightly increased when the interface height increased from 15-31 mm (i.e., Interfaces 10-14).

4.3.4 Effect of interface length

As shown in Fig. 21, impedance signatures in the range of 2-40 kHz were gained for the intact state from Interfaces 15-18 (see Table 3). Two resonant impedance peaks were observed as Peak 1 (5-17 kHz) and Peak 2 (20-35 kHz). Impedance frequencies of the two impedance peaks gradually decreased as the length of the flexible section varies from $L_f=20$ mm (Interface 15) to $L_f=32$ mm (Interface 18). Particularly, the real-impedance magnitude of Interface 15 was about twice smaller than that of Interface 18. The observation suggested that the slender interface yielded an excitation capacity of the PZT sensor. For the damage of Strand 1, Fig. 22 shows impedance signatures of Peak 1 zoomed for the range 0.6 kHz: 14.4-15 kHz for Interfaces 15 and 5.7-6.3 kHz for Interface 18. Interface 18's impedance signals were more sensitive than others were.

As shown in Fig. 23, RMSD indices of Interfaces 15-18' impedance responses were calculated for 0.6 kHz-bandwidth of Peak 1's impedance and 1.5 kHz-bandwidth of Peak 2's impedance. The RMSD indices of Peak 1 gradually increased along with the flexible-section length. Notably,

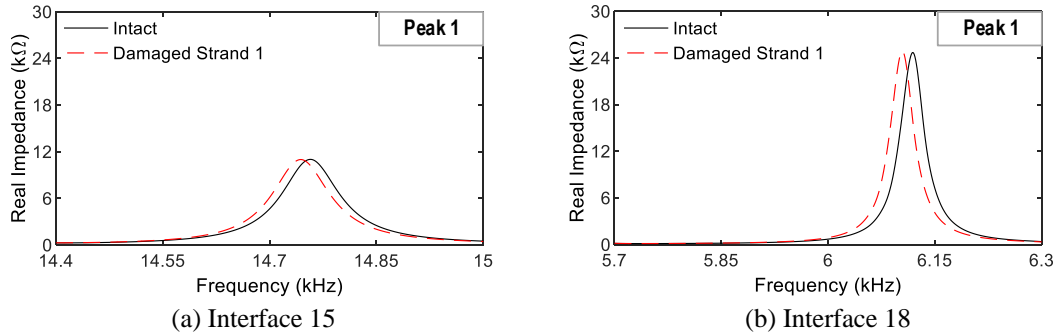


Fig. 22 Impedance signatures of Interfaces 15-18 zoomed in Peak 1's frequency range: Strand 1 breakage

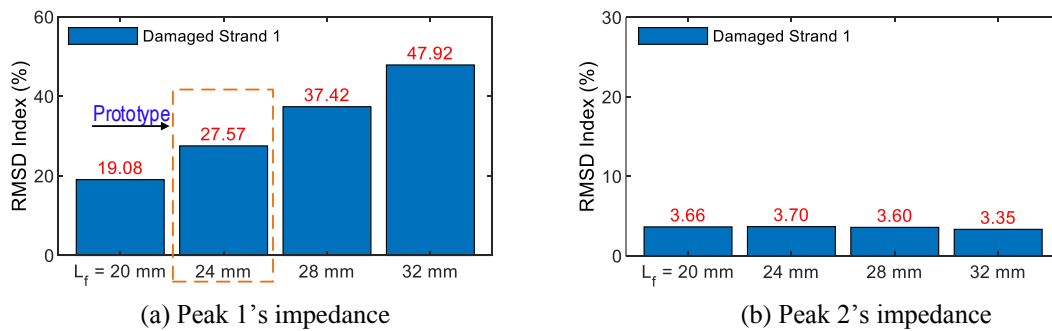


Fig. 23 Sensitivities of impedance signatures of Interfaces 15-18 for damage detection

Interface 18's RMSD value was about 1.7 times larger than that of Interface 17. Meanwhile, the RMSD magnitudes of Peak 2 was an ignorable change among Interfaces 15-18.

5. Experimental evaluation of various PZT interfaces for analyzing effects of material and geometric properties

5.1 Description of experiment

5.1.1 Test set-up

Various PZT interfaces were tested under compressive forces to evaluate the effects of the PZT interface's materials and sizes on sensitivities of impedance responses. It has been proved that more stress variation leads to more changes in impedance features (Lim *et al.* 2012, Ai *et al.* 2019, Dang *et al.* 2020a). Under a strand breakage event, it causes stress variation in the flexible section of the PZT interface, which can be reflected by changes in impedance features.

To analyze the sensitivities of various PZT interface's material and geometric parameters, the PZT interfaces were introduced with the same stress variation to acquire impedance signatures. Then, the RMSD index was utilized to analyze the effects of the PZT interface's materials and geometric constants. Fig. 24 shows the test set-up of the PZT interface, which was clamped in a compression tester. A series of compressive forces were controlled by a load cell, and the loading speed was set at about 0.02 mm/minute.

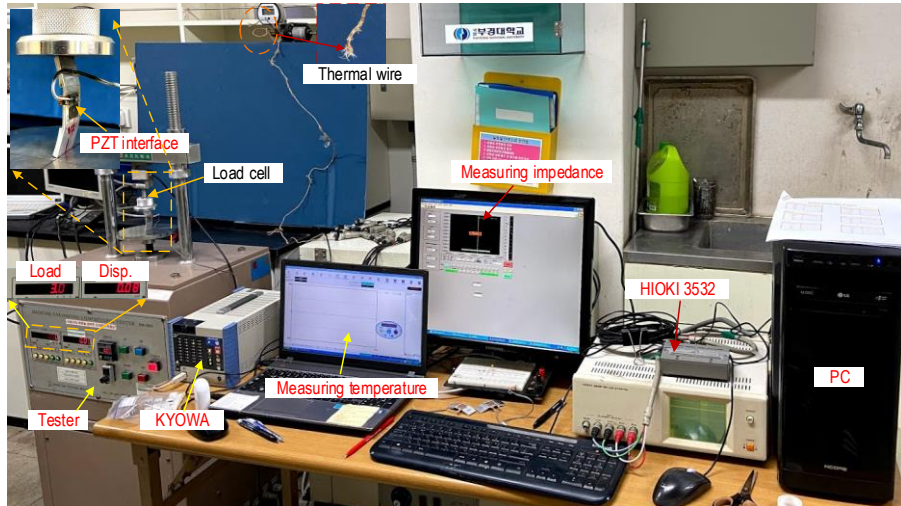


Fig. 24 Test set-up of PZT interface in compression tester for impedance measurement

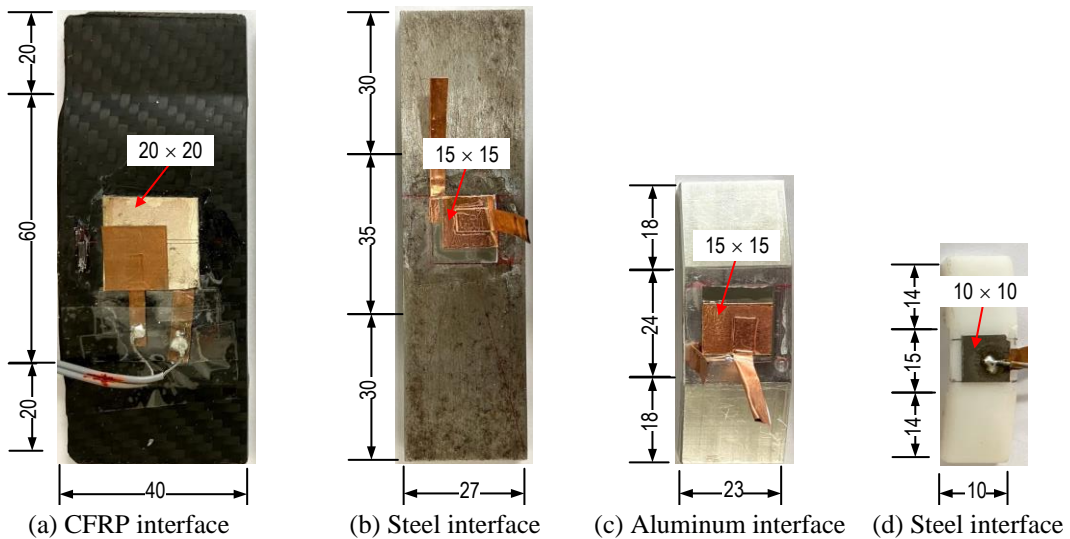


Fig. 25 Four different material types of PZT interfaces

To acquire impedance responses, an impedance analyzer (HIOKI 3532) was utilized to apply 1V-harmonic excitation and gain impedance signals from the PZT patch. Also, the EDX-100A was used to measure room temperatures via thermocouple wire (K-type). During the experiment, the variation of temperatures was less than 1°C (around 28°C), thus minimizing the effect of temperature variation on impedance features.

5.1.2 Four different material types of PZT interfaces

As shown in Fig. 25, four different types of PZT interfaces were tested to analyze the effects of interface materials on impedance responses. The four materials included CFRP (carbon fiber reinforced polymer), steel, aluminum, and polypropylene plastic. Design parameters of the four

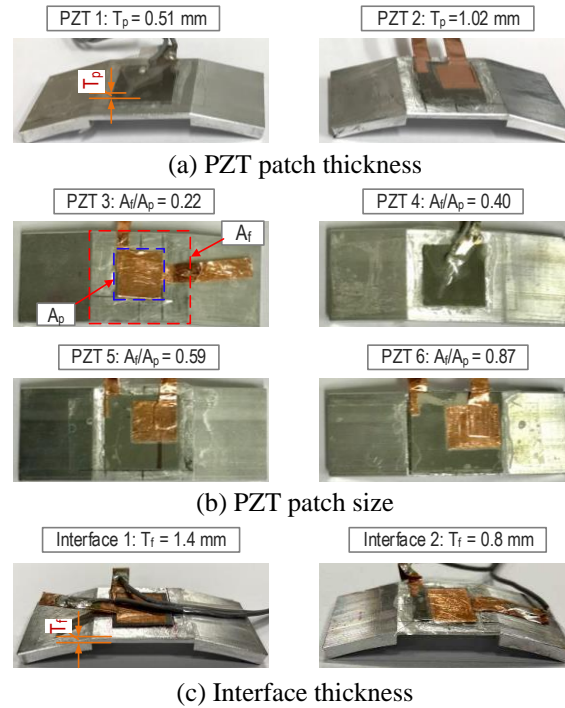


Fig. 26 Interface thickness, PZT-patch thickness, and PZT-patch covering area

PZT interfaces were specified as follows (see also Fig. 2(b)): a) the CFRP type had $H_{int} \times L_b \times T_b = 40 \times 20 \times 3 \text{ mm}^3$, $H_{int} \times L_f \times T_f = 40 \times 60 \times 3 \text{ mm}^3$, and $L_p \times H_p \times T_p = 20 \times 20 \times 0.51 \text{ mm}^3$; b) the steel type had $H_{int} \times L_b \times T_b = 27 \times 30 \times 5 \text{ mm}^3$, $H_{int} \times L_f \times T_f = 27 \times 35 \times 4 \text{ mm}^3$, and $L_p \times H_p \times T_p = 15 \times 15 \times 0.51 \text{ mm}^3$; c) the aluminum type had $H_{int} \times L_b \times T_b = 23 \times 18 \times 3.4 \text{ mm}^3$, $H_{int} \times L_f \times T_f = 23 \times 24 \times 1.4 \text{ mm}^3$, and $L_p \times H_p \times T_p = 15 \times 15 \times 0.51 \text{ mm}^3$; and d) the plastic PZT interface had $H_{int} \times L_b \times T_b = 10 \times 14 \times 3.4 \text{ mm}^3$, $H_{int} \times L_f \times T_f = 10 \times 15 \times 1.4 \text{ mm}^3$, and $L_p \times H_p \times T_p = 10 \times 10 \times 0.51 \text{ mm}^3$. The material properties of the four interfaces were listed in Table 1.

For the selected materials, the sensitivities of impedance responses were examined with respect to axial stresses applied to the interfaces, which could simulate real stress states in a prestressed tendon anchorage. The applied loads were chosen based on the yield strength of the plastic interface (see Table 1). The compressive stresses were simulated with five levels for impedance measurement. At first, a PZT interface was compressed by the stress of 0.25 MPa (S1) to make an initial state. Then, compressive stress was increased from 0.25-0.45 MPa (S1-S5) with an interval of 0.05 MPa.

5.2.3 PZT-patch thickness, PZT-patch coverage area, and interface thickness

As shown in Fig. 26, geometrical properties of PZT interfaces were examined for PZT-patch thickness, PZT-patch coverage area, and interface thickness. The aluminum interface shown in Fig. 25(c) was used as the baseline prototype. Firstly, the PZT-patch thickness (T_p) was tested for two cases: PZT 1 with 0.51 mm and PZT 2 with 1.02 mm. The PZTs 1 and 2 had the same size of 15×15 mm (see Fig. 26(a)). Secondly, the rate of the coverage area of the PZT patch (A_p) over the interface's flexible section (A_f) was tested for four cases: PZT 3 with 0.22, PZT 4 with 0.40, PZT 5 with 0.59, and PZT 6 with 0.87. Notably, PZTs 1-6 mounted on the baseline prototype had the same thickness

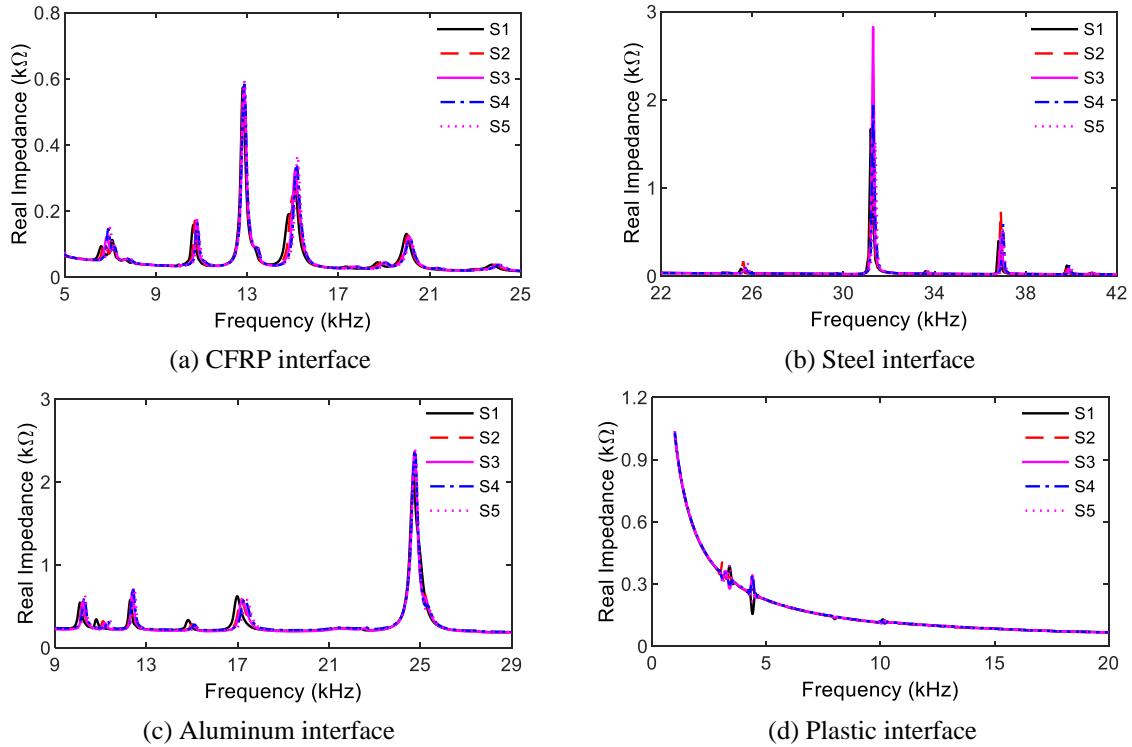


Fig. 27 Impedance responses of four interface materials under compression

of $T_f=1.4$ mm (see Fig. 26(a)-(b)). Thirdly, the interface thickness (T_f) of the flexible section was tested for two cases: Interfaces 1 with 1.4 mm and Interface 2 with 0.8 mm (see Fig. 26(c)).

Five levels of compressive forces (C1-C5) were designed to estimate the effect of the PZT interface’s geometry on the sensitivity of impedance responses. At first, a PZT interface was compressed by a force of 25 N to make an initial state (C1). Then, the compressive load was increased from 25-45 N (C1-C5) with an interval of 5.0 N. Note that structural damage caused the stress variation in the flexible-section interface as the PZT interface was mounted on a monitored structure. Consequently, the forces C1-C5 caused compressive stress 0.78-1.4 MPa for the interfaces with $T_f=1.4$ mm (i.e., PZT1-PZT6, Interface 1) and 1.36-2.45 MPa for the interface with $T_f=0.8$ mm (i.e., Interface 2, see Fig. 26(c)).

5.2 Effects of interface’s material properties for sensitive impedance responses

As shown in Figs. 27(a)-(d), impedance responses in the bandwidth of 20 kHz were measured from the CFRP, steel, aluminum, and plastic interfaces, respectively. The CFRP, steel, and aluminum interfaces had real impedance signals of clear resonant peaks; meanwhile, the plastic interface had unclear resonant impedance peaks (see Fig. 27(d)). The steel and aluminum interfaces had relatively high magnitudes of the real impedance signals. The real impedance signals were shifted under a series of compressive stresses.

As shown in Fig. 28(a), RSMD indices were computed to quantify the variation of impedance responses. For the four interfaces with different materials, the RMSD indices were calculated for

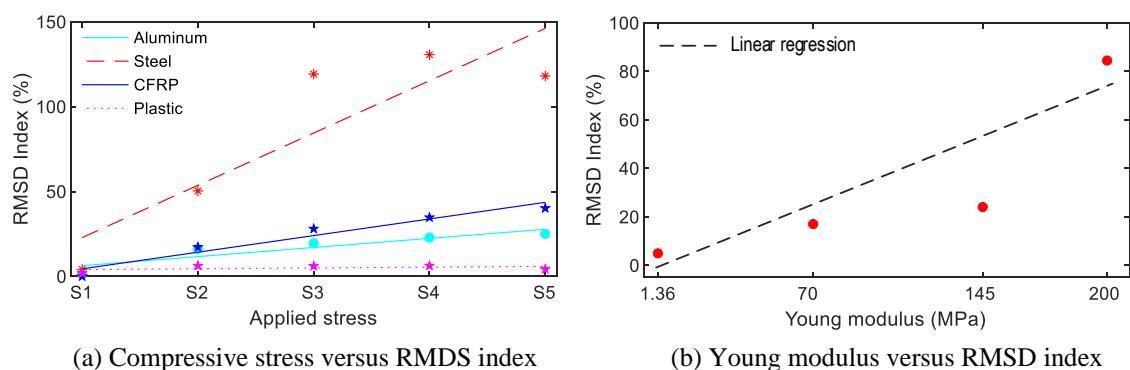


Fig. 28 Sensitivities of impedance responses of four interface materials for stress monitoring

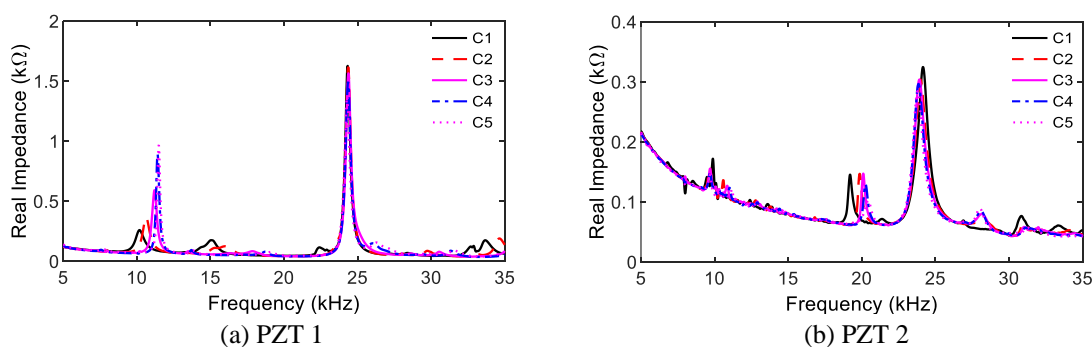


Fig. 29 Experimental impedance responses measured from different thicknesses of PZT sensors under compression

the 20 kHz-bandwidth of impedance signals. As the compressive loads increased from S1 (0.25 MPa) to S5 (0.45 MPa), the RMSD magnitudes of the CFRP, steel, and aluminum interfaces increased linearly. Meanwhile, the RMSD magnitude of the plastic interface almost no change. Moreover, Fig. 28(b) shows the relationship between the Young modulus and RMSD index calculated from average RMSD indices of test cases S1-S5. It reveals that a higher stiffness of interface yield a higher sensitivity. The experimental result shows a good agreement with the numerical simulation (see Fig. 5). It suggested that the plastic material should not be used for interface-based impedance measurement.

5.3 Effects of interface's geometric properties for sensitive impedance responses

5.3.1 Effect of PZT-patch thickness

Fig. 29 shows impedance responses of PZTs 1-2 in the range 5-35 kHz under compressive forces C1-C5. The impedance responses varied under increasing compression load. Also, the real impedance magnitudes of PZT 2 (thickness of 1.02 mm) were lower than that of PZT 1.

Fig. 30 shows the RMSD index calculated for the frequency range 5-35 kHz of PZTs 1-2. The RMSD magnitudes of PZTs 1-2 linearly increased with respect to the increasing forces C1-C5. There were slight differences in RMSD magnitudes of PZT 1 and PZT 2. The experimental results do not quite agree with the numerical analysis, in which the thinner PZT patch yielded the higher

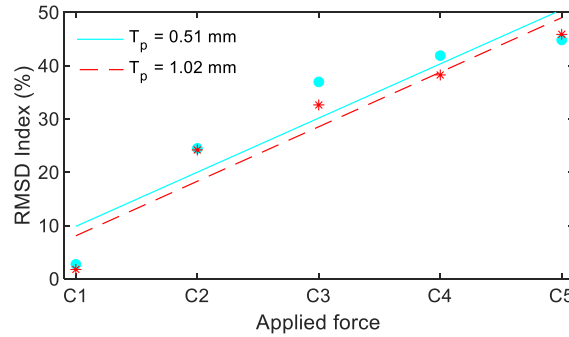


Fig. 30 Sensitivity of experimental impedance responses versus different thicknesses of PZT sensors under compression

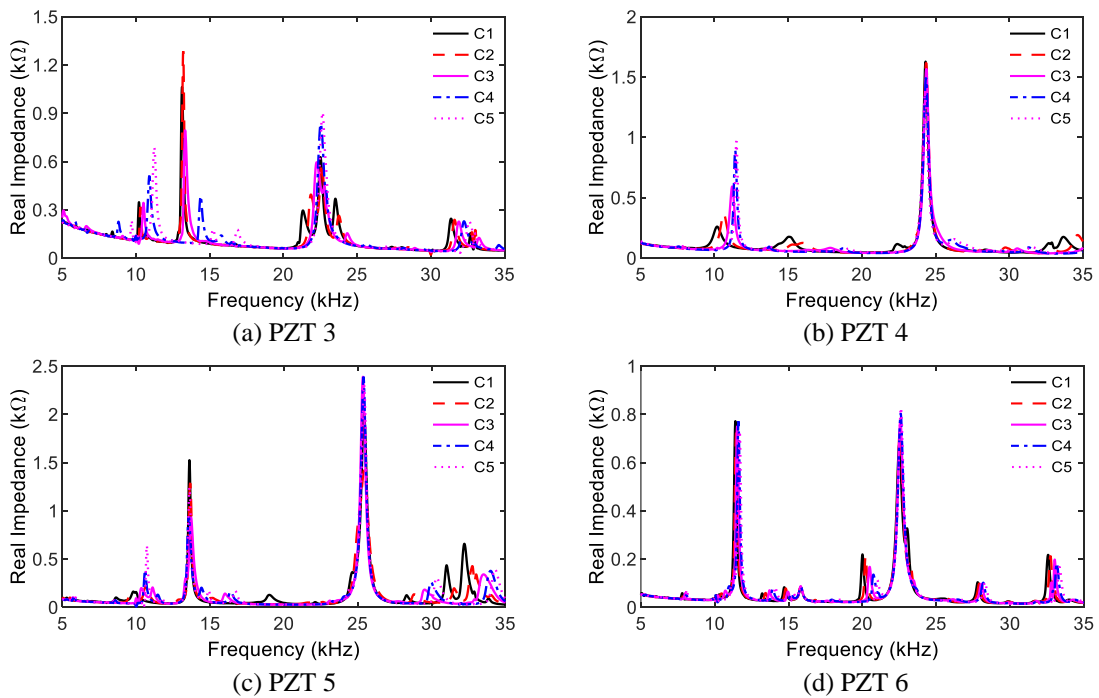


Fig. 31 Impedance responses of four PZT-patch sizes under compression

RMSD magnitude (see Fig. 8).

5.3.2 Effect of PZT-patch coverage area

As shown in Fig. 31, impedance responses were acquired from PZTs 3-6 in the range 5-35 kHz under the compressive load C1-C5. There were two clear resonant frequency peaks and some additional peaks in the examined frequency range. Fig. 32 shows the RMSD index of PZTs 3-6 calculated for the range 5-35 kHz. The RMSD magnitudes of PZTs 4-6 linearly increased with respect to increasing forces C1-C5. The RMSD magnitude of PZT 3, which had the smallest coverage area of the PZT sensor, had the largest values. It was indicated that the small size of the

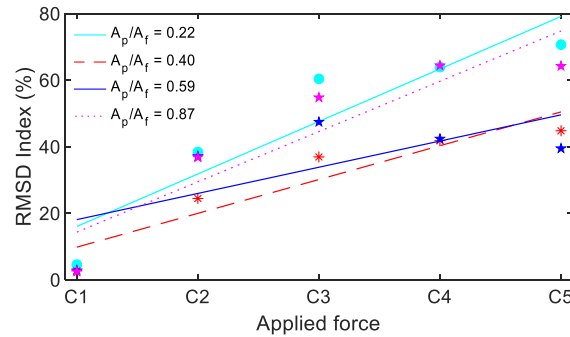


Fig. 32 Sensitivities of impedance responses of four PZT-patch sizes for stress monitoring

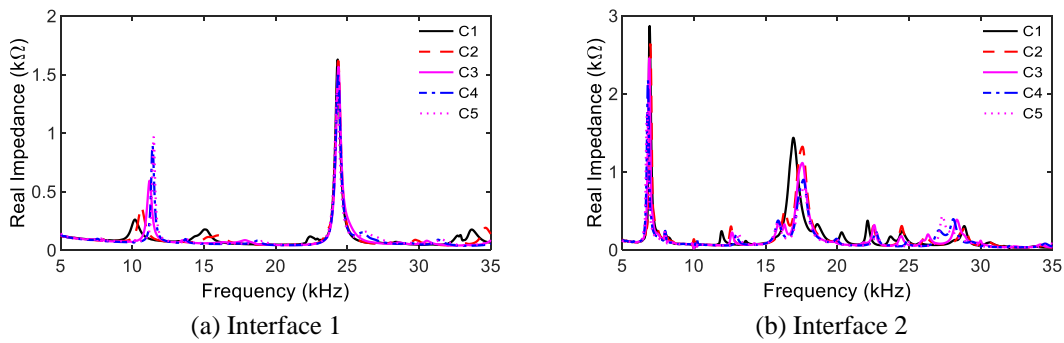


Fig. 33 Experimental impedance responses measured from different thicknesses of hoop interfaces under compression

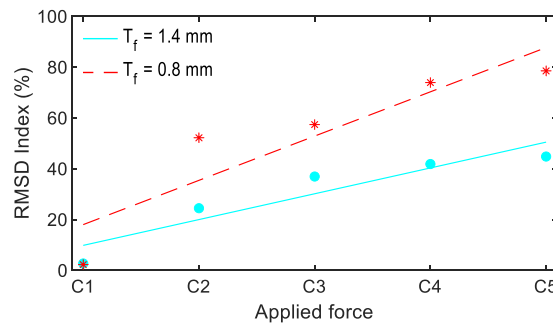


Fig. 34 Sensitivity of experimental impedance responses versus different thickness of hoop-interface under compression

PZT sensor yielded higher sensitivity of the impedance responses. The result shows a good agreement with the numerical analysis (see Fig. 10).

5.3.3 Effect of interface thickness

Fig. 33 shows impedance signatures acquired from Interfaces 1-2 in the range 5-35 kHz under compressive forces C1-C5. There were two clear resonant frequency peaks and some unclear peaks

in the examined frequency range. This is because the boundary condition of the interfaces in the experiment was slightly different from the numerical analysis. Interface 2's impedance signals show more sensitive to force variation than that of Interface 1.

Fig. 34 presents the RMSD indices of Interfaces 1-2 calculated for the frequency range 5-35 kHz. The RMSD magnitudes linearly increased with respect to increasing compressive load. The RMSD magnitudes of Interface 2 (0.8 mm thick) were higher than that of Interface 1. The thinner flexible section yielded a higher sensitivity of impedance responses. This observation shows a good agreement with the numerical analysis (see Fig. 14).

6. Conclusions

The parametric analysis was performed on the hoop-type PZT interface to analyze the effect of the PZT interface's material and geometric properties on the variation of impedance signatures induced by strand breakage. Firstly, the concept of impedance monitoring via the PZT interface technique was introduced. Secondly, the material properties and geometric properties of the PZT sensor and the interface body were numerically simulated to gain impedance signals under the strand breakage case. The RMSD damage metric was used to quantify the effect of those parameters on damage-sensitive impedance responses. Finally, the experiment evaluation was conducted on the PZT interfaces to support the numerical investigation.

From the numerical and experimental analyses, three concluding remarks were made as follows. Firstly, the stiffer interface material yielded greater changes in impedance signatures induced by damage occurrence. Secondly, the thickness of the interface's flexible section had the most effect on damage-sensitive impedance responses. For the detection of incipient damage in the anchorage, the 0.8 mm-thick flexible section was the pick for the hoop-type PZT interface. Lastly, a ratio of PZT sensor' area to the interface's flexible-section area should be selected about 0.4 to enlarge performance impedance-based damage detection for the tendon anchorage. This study provided a guideline for the selection of material and geometric constants of the PZT interface for the impedance-based damage detection in the tendon anchorage. As further work, the performance of the PZT interface with optimal parameters should be experimentally investigated on real-scale tendon anchorages under partially damaged strands. The effects of environmental parameters (e.g., temperature changes) is also recommended.

Author contributions

Methodology, N.L. D and J.T. K; software, investigation, and data curation, Q.Q, P and N.L.D; writing original draft, N.L. D; review, editing, and supervision, J.T. K.

Acknowledgments

This work was supported by a grant (21CTAP-C163708-01) from the Technology Advancement Research Program funded by Korea Agency for Infrastructure Technology Advancement (KAIA).

References

- Abdullah, A.B.M., Rice, J.A. and Hamilton, H.R. (2015), "Wire breakage detection using relative strain variation in unbonded posttensioning anchors", *J. Bridge Eng.*, **20**(1), 1-12. [https://doi.org/10.1061/\(ASCE\)BE.1943-5592.0000639](https://doi.org/10.1061/(ASCE)BE.1943-5592.0000639).
- Ai, D., Lin, C. and Zhu, H. (2020), "Embedded piezoelectric transducers based early-age hydration monitoring of cement concrete added with accelerator/retarder admixtures", *J. Intel. Mater. Syst. Struct.*, **32**(8), 847-866. <https://doi.org/10.1177/1045389X20969916>.
- Ai, D., Luo, H. and Zhu, H. (2019), "Numerical and experimental investigation of flexural performance on pre-stressed concrete structures using electromechanical admittance", *Mech. Syst. Signal Pr.*, **128**, 244-265. <https://doi.org/10.1016/j.ymsp.2019.03.046>.
- Ai, D., Luo, H., Wang, C. and Zhu, H. (2018), "Monitoring of the load-induced RC beam structural tension/compression stress and damage using piezoelectric transducers", *Eng. Struct.*, **154**, 38-51. <https://doi.org/10.1016/j.engstruct.2017.10.046>.
- Aloui, O., Lin, J. and Rhode-Barbarigos, L. (2019), "A theoretical framework for sensor placement, structural identification and damage detection in tensegrity structures", *Smart Mater. Struct.*, **28**(12), 125004-1-11. <https://doi.org/10.1088/1361-665X/ab3d21>.
- Asadollahi, P. and Li, J. (2017), "Statistical analysis of modal properties of a cable-stayed bridge through long-term wireless structural health monitoring", *J. Bridge Eng.*, **22**(9), 04017051-1-15. [https://doi.org/10.1061/\(ASCE\)BE.1943-5592.0001093](https://doi.org/10.1061/(ASCE)BE.1943-5592.0001093).
- Bachmann, H., Ammann, W.J., Deischl, F., Eisenmann, J., Floegl, I., Hirsch, G.H., ... & Steinbeisser, L. (2012), *Vibration Problems in Structures: Practical Guidelines*, Birkhäuser.
- Cervenka, V. and Ganz, H.R. (2014), "Validation of post-tensioning anchorage zones by laboratory testing and numerical simulation", *Struct. Concrete*, **15**(2), 258-268. <https://doi.org/10.1002/suco.201300038>.
- Dang, N.L., Huynh, T.C. and Kim, J.T. (2019), "Local strand-breakage detection in multi-strand anchorage system using an impedance-based stress monitoring method-feasibility study", *Sensor. (Basel)*, **19**(5), 1054. <https://doi.org/10.3390/s19051054>.
- Dang, N.L., Huynh, T.C., Pham, Q.Q., Lee, S.Y. and Kim, J.T. (2020a), "Damage-sensitive impedance sensor placement on multi-strand anchorage based on local stress variation analysis", *Struct. Control Hlth. Monit.*, **27**, e2547. <https://doi.org/10.1002/stc.2547>.
- Dang, N.L., Pham, Q.Q. and Kim, J.T. (2020b), "Piezoelectric-based hoop-type interface for impedance monitoring of local strand breakage in prestressed multi-strand anchorage", *Struct. Control Hlth. Monit.*, **28**(1), 1-20. <https://doi.org/10.1002/stc.2649>.
- Ferrari, R., Froio, D., Rizzi, E., Gentile, C. and Chatzi, E.N. (2019), "Model updating of a historic concrete bridge by sensitivity- and global optimization-based Latin Hypercube Sampling", *Eng. Struct.*, **179**, 139-160. <https://doi.org/10.1016/j.engstruct.2018.08.004>.
- Hamed, E. and Frostig, Y. (2006), "Natural frequencies of bonded and unbonded prestressed beams—prestressing force effects", *J. Sound Vib.*, **295**(1-2), 28-39. <https://doi.org/10.1016/j.jsv.2005.11.032>.
- He, L., Lian, J., Ma, B. and Wang, H. (2014), "Optimal multi-axial sensor placement for modal identification of large structures", *Struct. Control Hlth. Monit.*, **21**(1), 61-79. <https://doi.org/10.1002/stc.1550>.
- Hiba, A.J. and Glisic, B. (2019), "Monitoring of prestressing forces in prestressed concrete structures—An overview", *Struct. Control Hlth. Monit.*, **26**(8), e2374-1-27. <https://doi.org/10.1002/stc.2374>.
- Ho, D.D., Kim, J.T., Stubbs, N. and Park, W.S. (2012), "Prestress-force estimation in PSC girder using modal parameters and system identification", *Adv. Struct. Eng.*, **15**(6), 997-1012. <https://doi.org/10.1260/1369-4332.15.6.997>.
- Hou, R., Xia, Y., Xia, Q. and Zhou, X. (2019), "Genetic algorithm based optimal sensor placement for L1-regularized damage detection", *Struct. Control Hlth. Monit.*, **26**(1), e2274-1-14. <https://doi.org/10.1002/stc.2274>.
- Hu, W.H., Said, S., Rohrmann, R.G., Cunha, Á. and Teng, J. (2017), "Continuous dynamic monitoring of a prestressed concrete bridge based on strain, inclination and crack measurements over a 14-year span",

- Struct. Hlth. Monit.*, **17**(5), 1073-1094. <https://doi.org/10.1177/1475921717735505>.
- Huynh, T.C. and Kim, J.T. (2014), "Impedance-based cable force monitoring in tendon-anchorage using portable PZT-interface technique", *Math. Prob. Eng.*, **2014**, 1-11. <https://doi.org/10.1155/2014/784731>.
- Huynh, T.C. and Kim, J.T. (2017), "Quantitative damage identification in tendon anchorage via PZT interface-based impedance monitoring technique", *Smart Struct. Syst.*, **20**(2), 181-195. <https://doi.org/10.12989/sss.2017.20.2.181>.
- Huynh, T.C., Ho, D.D., Dang, N.L. and Kim, J.T. (2019), "Sensitivity of piezoelectric-based smart interfaces to structural damage in bolted connections", *Sensor. (Basel)*, **19**(19), 1-22. <https://doi.org/10.3390/s19173670>.
- Hwang, D., Kim, S. and Kim, H.K. (2021), "Long-term damping characteristics of twin cable-stayed bridge under environmental and operational variations", *J. Bridge Eng.*, **26**(9), 04021062-1-13. [https://doi.org/10.1061/\(ASCE\)BE.1943-5592.0001761](https://doi.org/10.1061/(ASCE)BE.1943-5592.0001761).
- Kim, J.M., Kim, H.W., Park, Y.H., Yang, I.H. and Kim, Y.S. (2012), "FBG sensors encapsulated into 7-wire steel strand for tension monitoring of a prestressing tendon", *Adv. Struct. Eng.*, **15**(6), 907-917. <https://doi.org/10.1260/1369-4332.15.6.907>.
- Kim, J.T., Park, J.H., Hong, D.S. and Park, W.S. (2010), "Hybrid health monitoring of prestressed concrete girder bridges by sequential vibration-impedance approaches", *Eng. Struct.*, **32**(1), 115-128. <https://doi.org/10.1016/j.engstruct.2009.08.021>.
- Kim, S.H., Park, S.Y. and Jeon, S.J. (2020), "Long-term characteristics of prestressing force in post-tensioned structures measured using smart strands", *Appl. Sci.*, **10**(12), 1-15. <https://doi.org/10.3390/app10124084>.
- Kim, S.W., Jeon, B.G., Kim, N.S. and Park, J.C. (2013), "Vision-based monitoring system for evaluating cable tensile forces on a cable-stayed bridge", *Struct. Hlth. Monit.*, **12**(5-6), 440-456. <https://doi.org/10.1177/1475921713500513>.
- Li, D., Tan, M., Zhang, S. and Ou, J. (2018), "Stress corrosion damage evolution analysis and mechanism identification for prestressed steel strands using acoustic emission technique", *Struct. Control Hlth. Monit.*, **25**(8), 1-11. <https://doi.org/10.1002/stc.2189>.
- Liang, C., Sun, F.P. and Rogers, C.A. (1994), "Coupled electro-mechanical analysis of adaptive material systems-determination of the actuator power consumption and system energy transfer", *J. Intel. Mater. Syst. Struct.*, **5**(1), 12-20. <https://doi.org/10.1177/1045389X9400500102>.
- Lim, Y.Y. and Soh, C.K. (2012), "Effect of varying axial load under fixed boundary condition on admittance signatures of electromechanical impedance technique", *J. Intel. Mater. Syst. Struct.*, **23**(7), 815-826. <https://doi.org/10.1177/1045389X12437888>.
- Lu, X., Lim, Y.Y. and Soh, C.K. (2018), "A novel electromechanical impedance-based model for strength development monitoring of cementitious materials", *Struct. Hlth. Monit.*, **17**(4), 902-918. <https://doi.org/10.1177/1475921717725028>.
- Mehrabi, A.B., Ligozio, C.A., Ciolko, A.T. and Wyatt, S.T. (2010), "Evaluation, rehabilitation planning, and stay-cable replacement design for the hale boggs bridge in Luling, Louisiana", *J. Bridge Eng.*, **15**(4), 364-372. [https://doi.org/10.1061/\(ASCE\)BE.1943-5592.0000061](https://doi.org/10.1061/(ASCE)BE.1943-5592.0000061).
- Min, J., Yun, C.B. and Hong, J.W. (2016), "An electromechanical impedance-based method for tensile force estimation and damage diagnosis of post-tensioning systems", *Smart Struct. Syst.*, **17**(1), 107-122. <https://doi.org/10.12989/sss.2016.17.1.107>.
- Moustafa, A., Niri, E.D., Farhidzadeh, A. and Salamone, S. (2014), "Corrosion monitoring of post-tensioned concrete structures using fractal analysis of guided ultrasonic waves", *Struct. Control Hlth. Monit.*, **21**(3), 438-448. <https://doi.org/10.1002/stc.1586>.
- Na, W.S. (2017), "Distinguishing crack damage from debonding damage of glass fiber reinforced polymer plate using a piezoelectric transducer based nondestructive testing method", *Compos. Struct.*, **159**, 517-527. <https://doi.org/10.1016/j.compstruct.2016.10.005>.
- Na, W.S. (2018), "Low cost technique for detecting adhesive debonding damage of glass epoxy composite plate using an impedance based non-destructive testing method", *Compos. Struct.*, **189**, 99-106. <https://doi.org/10.1016/j.compstruct.2018.01.053>.
- Nguyen, K.D. and Kim, J.T. (2012), "Smart PZT-interface for wireless impedance-based prestress-loss

- monitoring in tendon-anchorage connection”, *Smart Struct. Syst.*, **9**(6), 489-504. <https://doi.org/10.12989/sss.2012.9.6.489>.
- Ni, Y.Q., Xia, H.W., Wong, K.Y. and Ko, J.M. (2012), “In-service condition assessment of bridge deck using long-term monitoring data of strain response”, *J. Bridge Eng.*, **17**(6), 876-885. [https://doi.org/10.1061/\(ASCE\)BE.1943-5592.0000321](https://doi.org/10.1061/(ASCE)BE.1943-5592.0000321).
- Peeters, B. and De Roeck, G. (2001), “Stochastic system identification for operational modal analysis: a review”, *J. Dyn. Syst. Measure. Control*, **123**(4), 659-667. <https://doi.org/10.1115/1.1410370>.
- Plastics & Elastomers Selector, <https://omnexus.specialchem.com/>
- Ren, W.X., Chen, G. and Hu, W.H. (2005), “Empirical formulas to estimate cable tension by cable fundamental frequency”, *Struct. Eng. Mech. Mater.*, **20**(3), 363-380. <https://doi.org/10.12989/sem.2005.20.3.363>.
- Ryu, J.Y., Huynh, T.C. and Kim, J.T. (2017), “Experimental investigation of magnetic-mount PZT-interface for impedance-based damage detection in steel girder connection”, *Struct. Monit. Mainten.*, **4**(3), 237-253. <https://doi.org/10.12989/smm.2017.4.3.237>.
- Standards, C. (2009), *Design and Construction of Building Components with Fibre-Reinforced Polymers*, Mississauga, Ontario, Canada.
- Sun, F.P., Chaudhry, Z., Liang, C. and Rogers, C.A. (1995), “Truss structure integrity identification using PZT sensor-actuator”, *J. Intel. Mater. Syst. Struct.*, **6**(1), 134-139. <https://doi.org/10.1177/1045389X9500600117>.
- Tadros, M.K., Omaishin, N.A., Seguirant, S.J. and Gallt, J.G. (2003), *Prestress Losses in Pretensioned High-Strength Concrete Bridge Girders*, Transportation Research Board.
- Tian, Y., Zhang, C., Jiang, S., Zhang, J. and Duan, W. (2020), “Noncontact cable force estimation with unmanned aerial vehicle and computer vision”, *Comput.-Aid. Civil Infrastr. Eng.*, **36**(1), 73-88. <https://doi.org/10.1111/mice.12567>.
- Wu, J., Li, W. and Feng, Q. (2018), “Electro-mechanical impedance (EMI) based interlayer slide detection using piezoceramic smart aggregates-a feasibility study”, *Sensor. (Basel)*, **18**(10), 1-14. <https://doi.org/10.3390/s18103524>.
- Yan, T.H. and Lin, R.M. (2006), “General optimization of sizes or placement for various sensors/actuators in structure testing and control”, *Smart Mater. Struct.*, **15**(3), 724-736. <https://doi.org/10.1088/0964-1726/15/3/008>.
- Yang, D.H., Yi, T.H., Li, H.N. and Zhang, Y.F. (2018a), “Correlation-based estimation method for cable-stayed bridge girder deflection variability under thermal action”, *J. Perform. Constr. Facil.*, **32**(5), 04018070-1-10. [https://doi.org/10.1061/\(ASCE\)CF.1943-5509.0001212](https://doi.org/10.1061/(ASCE)CF.1943-5509.0001212).
- Yang, D.H., Yi, T.H., Li, H.N. and Zhang, Y.F. (2018b), “Monitoring and analysis of thermal effect on tower displacement in cable-stayed bridge”, *Measure.*, **115**, 249-257. <https://doi.org/10.1016/j.measurement.2017.10.036>.
- Yang, M., Gong, J. and Yang, X. (2020), “Refined calculation of time-dependent prestress losses in prestressed concrete girders”, *Struct. Infrastr. Eng.*, **16**(10), 1430-1446. <https://doi.org/10.1080/15732479.2020.1712438>.
- Yang, Y. and Miao, A. (2010), “Two-dimensional modeling of the effects of external vibration on the PZT impedance signature”, *Smart Mater. Struct.*, **19**(6), 1-7. <https://doi.org/10.1088/0964-1726/19/6/065031>.
- Yang, Y., Chadha, M., Hu, Z., Vega, M.A., Parno, M.D. and Todd, M.D. (2021), “A probabilistic optimal sensor design approach for structural health monitoring using risk-weighted f-divergence”, *Mech. Syst. Signal Pr.*, **161**. <https://doi.org/10.1016/j.ymsp.2021.107920>.
- Yang, Y., Lim, Y.Y. and Soh, C.K. (2008), “Practical issues related to the application of the electromechanical impedance technique in the structural health monitoring of civil structures: I. Experiment”, *Smart Mater. Struct.*, **17**(3), 035008-1-14. <https://doi.org/10.1088/0964-1726/17/3/035008>.
- Yao, Y. and Glisic, B. (2015), “Sensing sheets: Optimal arrangement of dense array of sensors for an improved probability of damage detection”, *Struct. Hlth. Monit.*, **14**(5), 513-531. <https://doi.org/10.1177/1475921715599049>.
- Zhang, S., Shen, R., Wang, Y., De Roeck, G., Lombaert, G. and Dai, K. (2020), “A two-step methodology for

cable force identification”, *J. Sound Vib.*, **472**, 115201-1-16. <https://doi.org/10.1016/j.jsv.2020.115201>.
Zhou, G.D., Yi, T.H., Zhang, H. and Li, H.N. (2015), “Optimal sensor placement under uncertainties using a nondirective movement glowworm swarm optimization algorithm”, *Smart Struct. Syst.*, **16**(2), 243-262. <https://doi.org/10.12989/sss.2015.16.2.243>.

TY